ENVIRONMENTAL RESEARCH
LETTERS

LETTER • OPEN ACCESS

Global convection-permitting model improves subseasonal forecast of plum rain around Japan

To cite this article: Jun Gu *et al* 2024 *Environ. Res. Lett.* **19** 104021

IOP Publishing Environ. Res. Lett. 19 (2024) 104021 https://doi.org/10.1088/1748-9326/ad71e2

ENVIRONMENTAL RESEARCH
LETTERS

RECEIVED
22 May 2024

REVISED
19 August 2024

ACCEPTED FOR PUBLICATION
21 August 2024

PUBLISHED
30 August 2024

LETTER

Global convection-permitting model improves subseasonal forecast of plum rain around Japan

Jun Gu[1], Chun Zhao[1,2,3,*], Mingyue Xu[1], Jiawang Feng[1], Gudongze Li[1], Yongxuan Zhao[1], Xiaoyu Hao[4], Junshi Chen[2,4] and Hong An[2,4,*]

[1] Deep Space Exploration Laboratory/School of Earth and Space Sciences, University of Science and Technology of China, Hefei, People's Republic of China
[2] Laoshan Laboratory, Qingdao, People's Republic of China
[3] CAS Center for Excellence in Comparative Planetology, University of Science and Technology of China, Hefei, People's Republic of China
[4] School of Computer Science and Technology, University of Science and Technology of China, Hefei, People's Republic of China
[*] Authors to whom any correspondence should be addressed.

E-mail: chunzhao@ustc.edu.cn and han@ustc.edu.cn

Keywords: subseasonal forecast, global convection-permitting model, plum rain, high resolution

Supplementary material for this article is available online

Abstract

In 2020 early summer, a historically severe rainy season struck East Asia, causing extensive damage to life and property. Subseasonal forecast of this event challenges the limits of rainy season predictability. Employing the integrated atmospheric model across scales and the Sunway supercomputer, we conducted ensemble one-month forecasts at global 3 km, variable 4–60 km, and global 60 km resolutions. The global convection-permitting forecast accurately captures the rainband, while other forecasts exhibited northward and weaker shifts due to the northward shifts of the atmospheric rivers over Japan, attributed to intensified Western North Pacific Subtropical High (WNPSH). Further, the double-ITCZ-like tropical rainfall pattern in Western Pacific in global convection-permitting forecast contributes to a more accurate WNPSH and rainband. In contrast, other forecasts show a single-ITCZ-like pattern in Western Pacific, leading to a northward-shifted WNPSH and rainband, advocating the importance of accurately representing tropical convections, as they can significantly affect mid-/high-latitude weather and climate.

1. Introduction

The plum rain, also known as Meiyu in China or Baiu in Japan, is a unique persistent precipitation phenomenon that occurs almost every year in East Asia from early June to mid-July (Pan *et al* 2023). The rainband generally extends from the middle and lower reaches of Yangtze River in China to the Kyushu Island of Japan (Tanaka 1992, Ding and Chan 2005). This enduring precipitation can lead to severe flooding and significant loss of life during active years. In 2020 summer, an unexpectedly long-persisting Meiyu season hit China (Xu *et al* 2021) and an enhanced Baiu season affected the Kyushu Island (Hirockawa *et al* 2020, Araki *et al* 2021), triggering devasting floods and landslides that caused loss of human life and property damage (Zhou *et al* 2021). The mechanism behind this severe rainy season has attracted researchers' interest and can be explained by subseasonal phase transition of North Atlantic Oscillation (Liu *et al* 2020), the super Indian Ocean Dipole (Takaya *et al* 2020), and sea surface temperatures (SST) anomalies in Indian Ocean (Tang *et al* 2021, Zhou *et al* 2021) and potentially the depression over Tibetan Plateau (Li *et al* 2023a). Such rainfall events are not isolated occurrences, but rather exhibit an intensifying potentially in the context of global warming. As the climate continues to change, the intensity of East Asian rainband has been proved to increase over the years using historical satellite products (Li *et al* 2023b). Accurately forecasting such extreme rainy season in advance also poses a significant challenge. The Japan Meteorological Agency reported inadequate performance, both deterministic and ensemble forecast, for the 2020 Kyushu heavy rain event (Duc *et al* 2021).

To mitigate the devastating effects of this long-term rainy season and implement adaptive emergency policies, subseasonal forecast in advance is important. The aforementioned mechanisms and such Pacific–Japan pattern teleconnection (Huang and Li 1989, Hu *et al* 2024) could prominently improve the predictability and reduce uncertainties of rainy season forecast. Previous studies have shown that the predictability of the subtropical high offers a promising future for monsoon precipitation, tropical cyclones and extreme rainfall (Huang and Li 1989, Wang *et al* 2013, Hu *et al* 2023) and is also linked to summer rainfall over Japan (Nagata and Mikami 2017). Nonetheless, with these methods giving instruction, simulating the Western North Pacific Subtropical High (WNPSH) remains challenging (Song and Zhou 2014, Li *et al* 2023c), and CMIP5 simulations show a northward tendency of the WNPSH, making it difficult to forecast WNPSH and, consequently, the rainband accurately on subseasonal timescales.

Recent studies to improve subseasonal forecast skills have focused largely on integrated Earth system models, air–sea interactions, larger ensemble size and higher horizontal resolution (Lang *et al* 2020, Woolnough *et al* 2024, National Academies of Sciences 2016, Wu *et al* 2021, Nie *et al* 2023), while subseasonal forecast at global convection-permitting scales has received less attention. The development of global convection-permitting (cloud-resolving) models (Satoh *et al* 2019) and the advent of exascale supercomputing (He *et al* 2023) have made global convection-permitting forecast feasible (Gu *et al* 2022), potentially providing a solution beyond the predictability of subseasonal to seasonal forecast (S2S) (Schneider *et al* 2017, Dueben *et al* 2020). Some cases have also shown the superiority with global convection-permitting simulations, indicating a promising future of global convection-permitting model but without detailed research on specific events (Caldwell *et al* 2021, Lang *et al* 2023). Even though the hardware and software have been prepared, computational efficiency and data input/output (I/O) burden should be addressed for longer simulation under global convection-permitting scales. By employing the separated-files I/O framework and multi-dimension parallel strategies, recent studies overcame the significant I/O bottleneck and achieved significant speedup under massive parallel execution (Gu *et al* 2022, Hao *et al* 2023) on the new Sunway supercomputer of China.

With the abundant computing power of supercomputer, one-month ensemble forecasts with global 3 km resolution enabled us to investigate subseasonal forecast skills for plum rain around Japan at global convection-permitting scales, and to examine how large-scale circulation influences small-scale processes and vice versa. In this study, a global uniform 3 km horizontal-resolution forecast (U3KM), a coarser 60 km horizontal-resolution forecast (U60KM), and a regionally refined mesh covering our region of interest with grid spacing spanning from 4 km to 60 km (V4KM) (see figure S1) are investigated, which aims to demonstrate the forecast skill of subseasonal precipitation and WNPSH at global convection-permitting resolution and the mechanisms leading to its overcoming performance against other resolutions. This study presents the first effort to forecast plum rain on subseasonal timescales using a global convection-permitting model. The results reveal that the plum rain is influenced by the tropical rainfall in Western Pacific, where the global convection-permitting model exhibits a double-ITCZ-like tropical rainfall pattern in Western Pacific (D-ITCZ-WP) pattern that contributes to the enhancement of plum rain. In contrast, the forecasts at coarser and variable resolutions exhibit weaker plum rainfall against the observations due to their single-ITCZ-like pattern in Western Pacific (S-ITCZ-WP) and northward expansion of WNPSH.

2. Model, data and methods

2.1. Model and experiments design

This study utilized the integrated atmospheric model across scales (iAMAS) system (Gu *et al* 2022, Feng *et al* 2023, Hao *et al* 2023), an online-coupled meteorology and chemical composition model that simulates meteorological fields and chemical compositions and their meteorological feedbacks simultaneously, to conduct subseasonal forecasts. iAMAS adopts the dynamical core of Model for Prediction Across Scales—Atmosphere (Skamarock *et al* 2012), and is developed with the architecture to be compliant to the new Sunway supercomputer of China. Aside from differences in horizontal resolution and resulting timestep for time integration, all forecasts use the same parameterizations (see table S1 for experimental details). To avoid the chaotic effects, ensemble forecasts were conducted, starting on 10 June 2020, and lasting for one month. The five ensemble members for each forecast vary solely in their initial time, with a 3 h interval between each member. SST and sea–ice cover are prescribed as surface boundary conditions and updated every 6 h.

2.2. Dataset

To investigate the historical early-summer rainband around Japan and evaluate the model forecasts, we utilized the bias-corrected, reprocessed CPC Morphing technique (CMORPH) dataset (Xie *et al* 2019) and Integrated Multi-satellitE Retrievals for GPM (IMERG) (Huffman *et al* 2023). The fifth generation of the ECMWF atmospheric reanalysis of the global climate (ERA5) provided the initialization conditions and lower boundary conditions for our forecasts (Hersbach *et al* 2020). Additionally, monthly averaged pressure level variables from ERA5 were used to validate the forecast results.

To further validate the simulated early summer rainband, we analyzed the monthly average precipitation outputs from several CMIP6 models (Eyring *et al* 2016) (listed in table S2) and high-resolution model intercomparison project (HiResMIP) models (Haarsma *et al* 2016) for their Historical and atmosphere model intercomparison project (AMIP) simulations during the early boreal summer from 2000 to 2014. The inclusion of AMIP and historical simulation results with CMIP6 models serves to illustrate the limitations of coarse-resolution simulations in capturing the plum rain, thereby highlighting the benefits of using global convection-permitting resolution. These selected models are shown at far distances in the model tree (Knutti *et al* 2013) of CMIP models to characterize the wide variety of models.

2.3. Diagnostic analysis

To alleviate the visualization burden imposed by high-resolution 3-dimension data and to facilitate comparison between the three different resolutions and ERA5 data, fields such as water vapor mixing ratio and vertical speed are horizontally interpolated to the ERA5 grid with a resolution of 0.25 × 0.25 degrees. Vertically integrated vapor transport (IVT) is adopted to analyze the water vapor transport and atmospheric rivers (ARs). The IVT is calculated by vertically integrating the moisture transport between 950 hPa and 300 hPa pressure levels following Ralph *et al* (2019) as

$$\mathrm{IVT} = \frac{1}{g}\sqrt{\left(\int_{950}^{300} qu\,\mathrm{d}p\right)^2 + \left(\int_{950}^{300} qv\,\mathrm{d}p\right)^2}$$

where q is the layer mean specific humidity, u and v are zonal and meridional winds, g is the acceleration due to gravity. Vertical levels used to calculate IVT are set at every 25 hPa from 950 hPa to 300 hPa. ARs were detected when IVT exceeds the threshold of $250\,\mathrm{kg\,m^{-1}\,s^{-1}}$ (Guan and Waliser 2015).

3. Results

3.1. Subseasonal forecasts of plum rain at different resolutions

Over the past decade, these early summer rainbands have been primarily oriented west–east, extending from 122 °E to 154 °E in longitude and situated between 25 °N to 35 °N in latitude, with their extreme precipitation frequently occurring over the Kyushu Island (see figures S2 and S3). In 2020, another historically severe rainband struck Japan, with the heaviest precipitation concentrated over the Kyushu Island, which was situated on the northern edge of the subtropical high (figures 1(a) and (b)). One-month long forecast with global uniform coarser resolution (U60KM) are unable to produce the intensity and location of rainfall, while resulting in a virtual Changma (Korea) rainy season in the Korean Peninsula (figure 1(c)). Traditionally, variable-resolution forecast with regional refinement covering the area of interest can improve the forecast capability of mesoscale weather systems. Nevertheless, such one-month long forecast with regional refinement at convection-permitting scale over the WNP (V4KM) fails to improve precipitation forecast in terms of intensity or location, producing similar results to U60KM (figure 1(d)). These northward rainbands can be associated with an intensified and northward expansion of the subtropical high (denoted by 588 dagpm line of 500 hPa geopotential height (GPH) fields), as compared to ERA5 (figure 1(a)). In addition to these forecasts, historical simulations across many models in CMIP5/6 also fail to capture the WNPSH and associated rainband (Liu *et al* 2014, Song and Zhou 2014, Cherchi *et al* 2018) during the early boreal summer. Selected historical and AMIP simulations (from 2000 to 2014) averaged over the period from 10 June to 10 July, fail to replicate a precipitation pattern like the observations (see figure S4). Even the HighResMIP, a CMIP6 subproject with a higher resolution, fails to capture this rainband over the Japan (see figure S5). These missing or northward rainbands in forecasts often coincide with an intensified and northward expansion of the WNPSH, and such phenomena are beyond the predictability of models potentially, falling into the domain of S2S (Ren *et al* 2023, Li *et al* 2023d).

Instead, ensemble monthly forecast conducted under a global 3 km horizontal resolution with five members (U3KM) produce a similar rainband to observation in terms of location and intensity, albeit weaker (figure 1(e)). The subtropical high north ridge line displays an evident southward shrink when compared to either V4KM or U60KM.

3.2. Regional thermodynamical characteristics of plum rain

To quantify the latitudinal discrepancies and northward shifts in precipitation distribution discussed above, the zonal average of monthly mean precipitation from 122° E to 154° E is calculated to examine the latitudinal precipitation distribution, as shown in figure 1(f). The V4KM and U60KM generated similar precipitation peaks around 35.5° N, exhibiting consistent variations but positioned approximately 5 degrees northward compared to CMORPH/IMERG. Additionally, their peak values were lower, around $9\ \mathrm{mm\ d^{-1}}$, while CMORPH/IMERG showed a higher peak of around $13\ \mathrm{mm\ d^{-1}}$. In contrast, the U3KM accurately captures the latitudinal distribution,

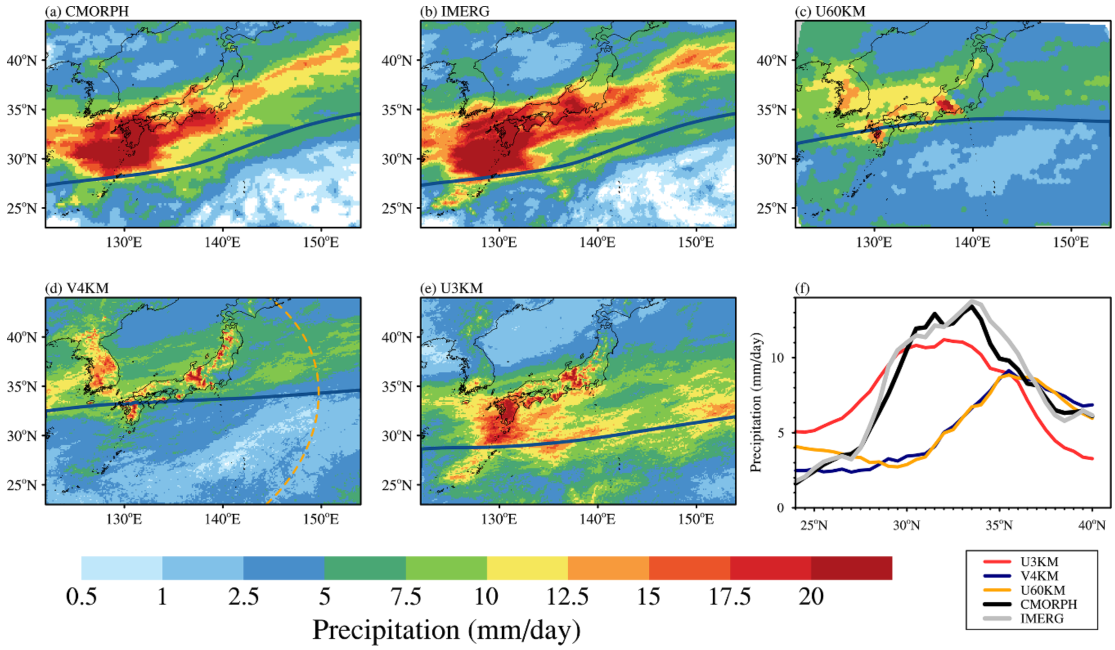

Figure 1. Panel (a), (b) show the monthly mean precipitation from CMORPH and IMERG, respectively (10 June to 10 July 2020). Panel (c), (d), and (e) depict the monthly mean precipitation from U60KM, V4KM and U3KM forecasts, respectively. The blue solid line indicates the 588 dagpm line of 500 hPa GPH of ERA5 (a), (b), U60KM (c), V4KM (d) and U3KM (e). The orange dashed elliptical curve defined the boundary between the refined region and the transition zone in V4KM mesh. Panel (f) shows the latitudinal profile of zonal-average (122° E–154° E) monthly mean precipitation.

reproducing the peak location and variation consistent with CMORPH/IMERG, albeit with slightly reduced intensity of 2 mm d^{-1} (figure 1(f)).

To further investigate the distribution differences locally, we present height-latitudinal cross-sections to illustrate the differences in water vapor and vertical velocity between U3KM and U60KM (figure 2(a)), V4KM and U60KM (figure 2(b)), and U3KM and V4KM (figure 2(c)). In figure 2(a), the U3KM simulates higher water vapor concentration southward of 30 °N throughout the troposphere, with a maximum difference of above 50% at 450 hPa. Coupled with stronger upward motion around 30° N, these conditions lead to higher instability and increased precipitation in this region for the U3KM. In contrast, V4KM shows a less than 10% increase in water vapor at mid-troposphere and 10% decrease at lower and higher atmosphere, with less intense downward and upward motion at 35° N compared to U60KM in upper and lower atmosphere, respectively (figure 2(b)). Despite these minor differences, the V4KM shows similar results to the U60KM in this region during the one-month forecast. The minor differences in water vapor and vertical velocity also reveal no apparent correlation with resolution in this region of analysis during the one-month forecast. Figure 2(c) reveals analogous patterns of difference, with the U3KM-V4KM comparison showing maximum differences at higher altitudes compared to U3KM-U60KM. Though the similar horizontal resolutions over the analysis region, the water vapor and vertical velocity fields display significant differences at various altitudes and latitudes, resulting in substantial precipitation discrepancy. These differences can be attributed to variations in the large-scale circulation systems beyond the refined region in V4KM, such as the East Asian monsoon and WNPSH. Overall, these results suggest that refining the resolution only in the region of interest for subseasonal forecasts may not necessarily improve the forecast capability, as demonstrated by the shorter time forecasts (Davis *et al* 2016, Xu *et al* 2021).

We also examine the ARs and their influence on precipitation, given their significant contribution (approximately 80%) to the boreal summer rainy season of 2020 (Wang *et al* 2021). Figure 3 illustrates the IVT and its zonal and meridional components using color-filled contours and vectors, respectively. Water vapor originates from the Indian Ocean south of 20° N, veering northward in the South China Sea (SCS), and intensifying around 30° N, coinciding with the peak rainfall location in U3KM (figure 3(b)) similar to ERA5 (figure 3(a)) albeit weaker. While both V4KM and U60KM exhibit enhanced intensity and more northward IVT in the SCS, corresponding to the AR's directional shift from eastward to northward. This intensity and direction remain consistent across the AR's eastward turn in mid-latitudes, leading to northward rainband around Japan (figure 3(c), (d)). Despite the mainstream of ARs occurring within the refined region of V4KM, V4KM shows no significant differences compared to U60KM. Moreover, the region where the AR turns northward in the SCS exhibits substantial differences, with each model

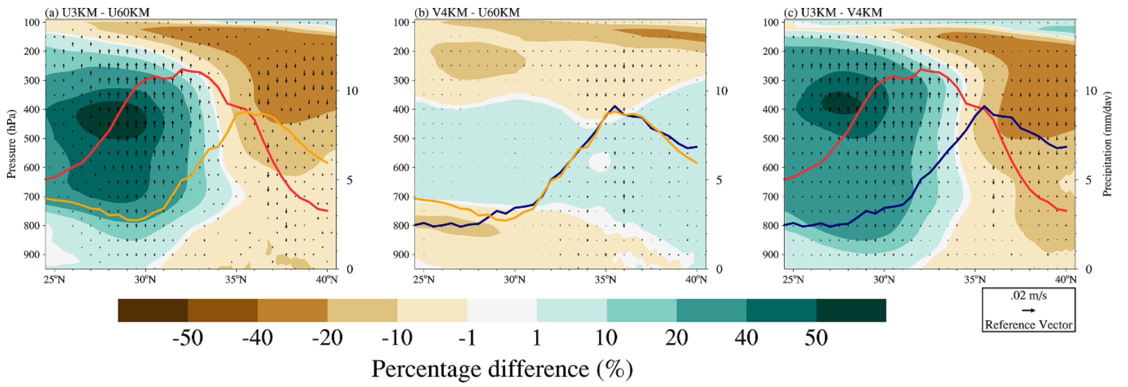

Figure 2. The three panels display the vertical profiles of the percentage change in water vapor mixing ratio (shaded) and the absolute differences in vertical speed (vectors) between: (a) U3KM and U60KM, (b) V4KM and U60KM, and (c) U3KM and V4KM, where the colored curves represent the latitudinal rainfall profiles of each resolution, as denoted in figure 1(f).

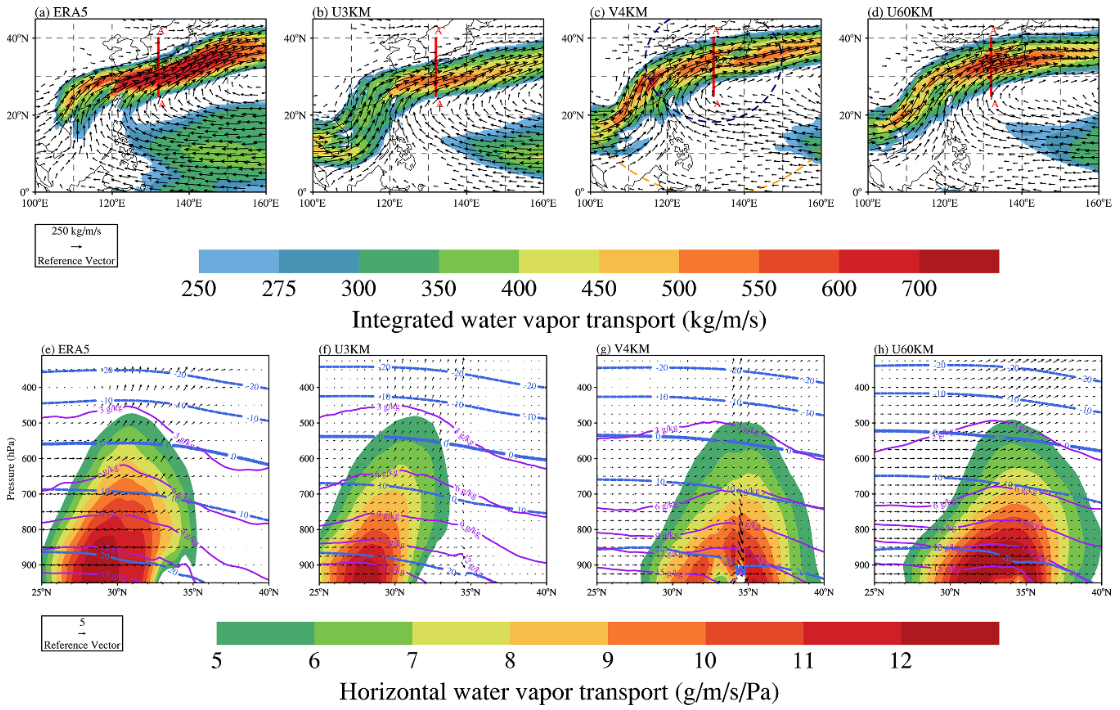

Figure 3. The top panels show the IVT (shaded) and its zonal and meridional components (vectors) average over one-month (a) ERA5 and forecasts of each resolution: (b) U3KM, (c) V4KM and (d) U60KM. The bottom panels display cross-sections along 133° E (marked as red lines A–A' in the top panels) of horizontal water vapor transport (shaded), temperature (blue dashed contour lines), specific humidity (purple solid contour lines) and meridional wind (vectors) for (e) ERA5, (f) U3KM, (g) V4KM and (h) U60KM.

having different horizontal resolutions in that region: U3KM at 3 km, U60KM at 60 km, and V4KM at the region transition zone from 4 km to 60 km. The resolution differences significantly influence the interaction between multiscale atmospheric systems, suggesting that biases from coarser resolutions can affect the weather systems in refined region at convection-permitting scale during long-term forecasts.

It is particularly noteworthy to examine the vertical structure of ARs at 133° E from 25° N to 40° N. U3KM exhibits a pronounced skewness in its vertical distribution, akin to a warm front, with the AR core centered around 28° N (figure 3(f)), aligning well with the water vapor transport depicted in figure 3(b) and ERA5 (figure 3(e)). In V4KM and U60KM, the AR core is located further northward, with V4KM showing weaker AR (figures 3(g) and (h)). The diminished AR activity at lower atmosphere around 34° N in V4KM can be attributed to the complex terrain on land, which is more resolved compared to U60KM, leading to complicated and higher terrain and downward vertical motion at this location, thereby reducing rainfall intensity. In terms of temperature, U3KM produces colder temperature and less water vapor in the lower atmosphere and low latitude, contrasting with the warmer and wetter air

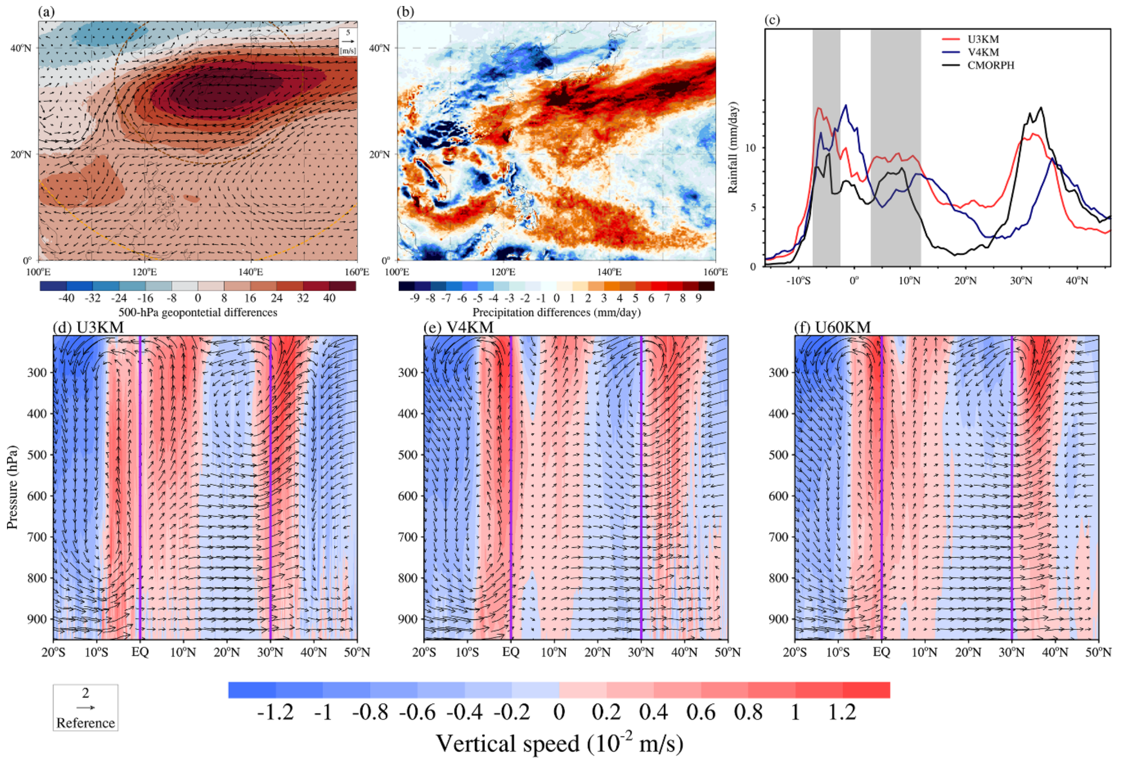

Figure 4. Panel (a) shows the monthly mean 500 hPa GPH and 850 hPa wind differences between V4KM and U3KM. Panel (b) presents the monthly mean precipitation differences between U3KM and V4KM. Panel (c) depicts the latitudinal profile of zonal-average (122° E–154° E) monthly mean precipitation. Panels (d)–(f) display the latitude-pressure sections of the zonal-mean meridional and vertical winds, with vertical wind speed being multiplied by 200 for visibility. The purple vertical lines denote the location of equator and 30° N, respectively.

in V4KM and U60KM (figures 3(f)–(h)). This discrepancy might be associated with the more intense WNPSH and the northward transport of water vapor in V4KM and U60KM.

3.3. Teleconnection with tropical rainfall

To elucidate the northward shift of AR in the SCS, as observed in both V4KM and U60KM, examinations of the dynamic and thermodynamic differences are essential. Figure 4(a) displays the differences in the 850 hPa wind fields between V4KM and U3KM, revealing that V4KM generates significant northward winds, propelling ARs in the same direction. This pattern is accompanied by an anticyclonic circulation, corresponding to reduced precipitation in this region (figure 4(b)). In U3KM, the enhancement of atmospheric instability, resulting from the increased latent heat release due to heavier rainfall, fosters convective processes, triggering lower-level convergence and intensified cyclonic winds aligning well with convective instability of the second kind (Charney and Eliassen 1964), hence not contributing to the northward of AR like in V4KM. The subtropical high also significantly influences the AR's latitudinal position, especially in the WNP where ARs predominantly occur north of the subtropical high. U60KM and V4KM generate a more intense subtropical high and stronger anticyclonic winds in the WNP, shifting the AR core's latitude northward and, consequently, the rainfall location. Notably, U3KM produces abundant rainfall in the SCS and Philippine Sea (figure 4(b)), creating a D-ITCZ-WP rainfall pattern similar to CMORPH (figure 4(c)). In contrast, V4KM and U60KM exhibit less off-equatorial precipitation, peaking at the equator, which aligns with previous findings (Landu *et al* 2014), where high-resolution aquaplanet simulations produce a double ITCZ, whereas coarser resolutions yield a single ITCZ pattern.

The ITCZ plays a crucial role in the Hadley cell (HC) as its ascending branch. To assess changes in the HC and other vertical meridional circulations, vertical cross-sections averaged from 122° to 154° are presented. The latitude profiles of rainfall correlate well with changes in vertical velocity across latitudes in each experiment (figure 4(c)–(f)). U3KM exhibits strong upward motion approximately 5 degrees south of the equator, extending from the surface to higher altitudes, with another ascending branch around 0–10° N where maximum upward motion occurs at higher altitudes (figure 4(d)). V4KM and U60KM present similar rainfall and meridional circulation profiles, with the most intense rainfall and upward motion at the equator, contrasting with U3KM's southward-to-equator pattern. Another ascending branch north of equator shows a northward tendency but weaker than that in U3KM, reflected in the reduced rainfall in these areas (figures 4(e) and (f)). Differences in the ascending branches of circulation over the equator result in distinct rainfall patterns, with U3KM producing a D-ITCZ-WP rainfall pattern, unlike V4KM and U60KM. The ascending branch circulation around mid-latitude (30° N) corresponding to rainfall around Japan exhibits significant discrepancies, with the branch is more northward in U60KM and V4KM, contributing to the northward rainband. The coarser-resolution forecast's more northward positioning of this branch underpins the rainbands around Japan and coincide with the S-ITCZ-WP rainfall pattern. Apart from the differences in rainfall location, both V4KM and U60KM also fail to generate rainfall as intense as U3KM, particularly considering the intense AR transport. U3KM can induce stronger upward motion and deep convection, leading to heavier rainfall, a capability not as pronounced in V4KM and U60KM.

The energetic framework for analyzing the HC, a popular method for explaining the position of meridional circulation, supports our finding. Here, we utilize the moist static energy (MSE) flux to offer energetic insights that corroborate our circulation analysis. As previously studied (Hill *et al* 2015, Wang *et al* 2023), the maximum of MSE flux marks the ascending branch of circulation. Our analysis shows that U3KM peaks at 30° N, while V4KM and U60KM peak at 35° N (see figure S6). Our circulation analysis aligns well with this energetic framework, providing further insights into why regional refinement and coarse resolution forecasts position the rainband more northward than observation, while U3KM does not.

4. Discussion and summary

Utilizing the 2020 plum rain case study, this study examines the advantages and reasons behind global convection-permitting model's accurate forecasting of the early summer rainband around Japan compared to global coarse- and variable-resolution forecast. The global convection-permitting forecasts better capture the observed rainfall distributions. In contrast, the long-term forecasts with global variable-resolution and coarse-resolution exhibit similar precipitation patterns and large-scale circulation systems but deviated from observation, indicating that biases from larger-scale circulation can significantly influence and control the smaller scales of the refined regions over extended forecast time, potentially mitigating the benefits of convection-permitting at regional scale.

Our findings underscore the WNPSH's critical role in modulating the rainband around Japan, occurring north of WNPSH's north ridge line. The U3KM accurately capture the WNPSH's north ridge line, aligning well with reanalysis data, whereas V4KM and U60KM exhibit a notable five-degree northward shift, leading to differences in the rainfall band's position and intensity. By investigating AR tracks and tropical rainfall disparities, we find that the latitudinal locations of AR turning points are influenced by rainfall in the SCS and Philippine Sea. The northward and intensified WNPSH in V4KM and U60KM corresponds to a S-ITCZ-WP rainfall pattern, while U3KM exhibits a D-ITCZ-WP pattern, with substantial rainfall in south of the equator, the SCS and Philippine Sea. The off-equatorial rainfall and upward motion influence the location and intensity of the WNPSH, contributing to U3KM's accurate rainband presentation that aligns well with observations, demonstrating the importance of tropical rainfall in shaping global weather and climate. Figure 5 summarizes and conceptualizes these complex interactions between tropical rainfall patterns, the WNPSH, and the resulting rainband around Japan. Beyond this specific case, we analyzed historical CMORPH and IMERG data to examine the relationship between tropical rainfall and latitudinal position of plum rain. We compared rainfall-weighted average latitudinal position (from 25° N to 40° N) against the off-equatorial tropical rainfall intensity (averaged over 7.5° S–2.5° S and 3° N–12° N, denoted by the gray shading in figure 4(c)) in the region from 122° E to 140° E. Results show that a less intense off-equatorial tropical rainfall corresponds to a higher latitudinal position of the plum rain (V4KM, U60KM), while a more intense tropical rainfall tends to be associated with a lower latitudinal position (U3KM, CMORPH and IMERG) (see figure S7). This observation-based pattern aligns with our conclusions, further supporting the link between tropical convection and latitudinal position of plum rain around Japan.

Nonetheless, there are some limitations to our study. Our analysis primarily focuses on horizontal resolution impacts on forecast results, highlighting the advantages of global convection-permitting forecasts, while not comprehensively investigating the sensitivity to model physics parameterization. Additionally, the choice of refined region and mesh size can influence the forecast results, as enlarging the refined region to cover tropical and critical areas discussed above could potentially improve the forecasts. The implications of these sensitivities warrant further exploration. Moreover, the influence of air–sea coupling processes on our results also warrants further investigation and model development. While some research efforts, such as the second phase of the DYAMOND project (Stevens *et al* 2019) (DYAMOND Winter), have used global convection-permitting atmospheric models coupled with global eddy-resolving ocean models for 40 d simulations, the potential improvements in subseasonal forecast

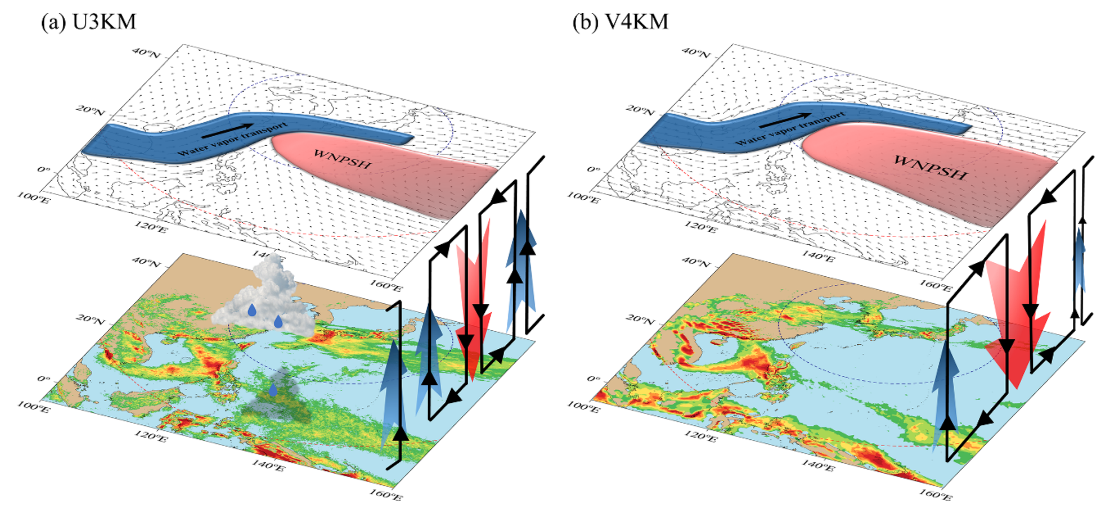

Figure 5. Schematic of the teleconnection between plum rain around Japan with tropical rainfall for (a) U3KM and (b) V4KM. The lower panels indicate the monthly mean rainfall (shaded). The upper panels show 850 hPa wind field (vectors) overlaid with the conceptual water vapor transport (blue shape) and WNPSH (pink shape). The blue arrows indicate the lifting motion of air, while the red arrows represent the sinking motion of air.

capabilities using such high-resolution coupled models remain an area for future research. Overall, global convection-permitting forecasts demonstrate strong prediction skills for subseasonal plum rain and subtropical highs, offering a promising path forward enhancing S2S forecasting capabilities, particularly in the context of warming climate. Nevertheless, challenges remain in accurately representing the intensity of such events, underscoring the need for continued model development and optimization.

Data availability statement

The data that support the findings of this study are openly available at the following URL/DOI: https://doi.org/10.5281/zenodo.13210739. The CMIP6 outputs of Historical and AMIP simulations are available at https://esgf-node.llnl.gov/search/cmip6/. The CMIP6 models used in this study can be found in table S2 of the Supporting Information. The CMORPH precipitation product is available at www.ncei.noaa.gov/data/cmorph-high-resolution-global-precipitation-estimates/access/30min/8km/2020. The IMERG precipitation product is available at https://disc.gsfc.nasa.gov/datasets/GPM_3IMERGDF_07/summary/. The ERA5 reanalysis dataset is available at https://doi.org/10.24381/cds.bd0915c6 for pressure levels and at https://doi.org/10.24381/cds.adbb2d47 for surface level.

Acknowledgments

This research was supported by the Strategic Priority Research Program of Chinese Academy of Sciences (XDB0500303), the Natural Science Foundation of Anhui (2208085UQ09, 2208085UQ02), the USTC Research Funds of the Double First-Class Initiative (YD2080002007, KY2080000114), the Science and Technology Innovation Project of Laoshan Laboratory (LSKJ202300305), and the National Key Scientific and Technological Infrastructure project 'Earth System Numerical Simulation Facility' (EarthLab). The study used the computing resources from the Supercomputing Center of the University of Science and Technology of China (USTC) and the Qingdao Supercomputing and Big Data Center. The authors also thank the Copernicus Climate Change Service (C3S) providing user-friendly and high-quality ERA5 data.

ORCID iDs

Jun Gu https://orcid.org/0000-0001-6129-3191
Chun Zhao https://orcid.org/0000-0003-4693-7213
Mingyue Xu https://orcid.org/0000-0002-8118-7908
Yongxuan Zhao https://orcid.org/0009-0000-7521-1791

References

Araki K, Kato T, Hirockawa Y and Mashiko W 2021 characteristics of atmospheric environments of quasi-stationary convective bands in Kyushu, Japan during the July 2020 heavy rainfall event *SOLA* **17** 8–15

Caldwell P M *et al* 2021 Convection-permitting simulations with the E3SM global atmosphere model *J. Adv. Model. Earth Syst.* **13** e2021MS002544

Charney J G and Eliassen A 1964 On the growth of the hurricane depression *J. Atmos. Sci.* **21** 68–75

Cherchi A, Ambrizzi T, Behera S, Freitas A C V, Morioka Y and Zhou T 2018 The response of subtropical highs to climate change *Curr. Clim. Change Rep.* **4** 371–82

Davis C A, Ahijevych D A, Wang W and Skamarock W C 2016 Evaluating medium-range tropical cyclone forecasts in uniform- and variable-resolution global models *Mon. Weather Rev.* **144** 4141–60

Ding Y and Chan J C L 2005 The East Asian summer monsoon: an overview *Meteorol. Atmos. Phys.* **89** 117–42

Duc L, Kawabata T, Saito K and Oizumi T 2021 Forecasts of the July 2020 Kyushu heavy rain using a 1000-member ensemble Kalman filter *SOLA* **17** 41–47

Dueben P D, Wedi N, Saarinen S and Zeman C 2020 Global simulations of the atmosphere at 1.45 km grid-spacing with the integrated forecasting system *J. Meteorol. Soc. Japan* II **98** 551–72

Eyring V, Bony S, Meehl G A, Senior C A, Stevens B, Stouffer R J and Taylor K E 2016 Overview of the coupled model intercomparison project phase 6 (CMIP6) experimental design and organization *Geosci. Model Dev.* **9** 1937–58

Feng J, Zhao C, Du Q, Xu M, Gu J, Hu Z and Chen Y 2023 Simulating atmospheric dust with a global variable-resolution model: model description and impacts of mesh refinement *J. Adv. Model. Earth Syst.* **15** e2023MS003636

Gu J *et al* 2022 Establishing a non-hydrostatic global atmospheric modeling system at 3-km horizontal resolution with aerosol feedbacks on the Sunway supercomputer of China *Sci. Bull.* **67** 1170–81

Guan B and Waliser D E 2015 Detection of atmospheric rivers: evaluation and application of an algorithm for global studies *J. Geophys. Res. Atmos.* **120** 12514–35

Haarsma R J *et al* 2016 High resolution model intercomparison project (HighResMIP v1.0) for CMIP6 *Geosci. Model Dev.* **9** 4185–208

Hao X, Fang T, Chen J, Gu J, Feng J, An H and Zhao C 2023 swMPAS-A: scaling MPAS-A to 39 million heterogeneous cores on the new generation Sunway supercomputer *IEEE Trans. Parallel Distrib. Syst.* **34** 141–53

He X *et al* 2023 Scalability and efficiency challenges for the exascale supercomputing system: practice of a parallel supporting environment on the Sunway exascale prototype system *Front. Inf. Technol. Electron. Eng.* **24** 41–58

Hersbach H *et al* 2020 The ERA5 global reanalysis *Q. J. R. Meteorol. Soc.* **146** 1999–2049

Hill S A, Ming Y and Held I M 2015 Mechanisms of forced tropical meridional energy flux change *J. Clim.* **28** 1725–42

Hirockawa Y, Kato T, Araki K and Mashiko W 2020 Characteristics of an extreme rainfall event in Kyushu district, Southwestern Japan in early July 2020 *SOLA* **16** 265–70

Hu P, Chen W, Chen S, Yang R, Wang L and Liu Y 2024 Revisiting the linkage between the pacific–Japan pattern and Indian summer monsoon rainfall: the crucial role of the maritime continent *Geophys. Res. Lett.* **51** e2023GL106982

Hu S, Zhou T, Wu B and Chen X 2023 Seasonal prediction of the record-breaking northward shift of the western Pacific subtropical high in July 2021 *Adv. Atmos. Sci.* **40** 410–27

Huang R and Li L 1989 Numerical simulation of the relationship between the anomaly of subtropical high over East Asia and the convective activities in the western tropical Pacific *Adv. Atmos. Sci.* **6** 202–14

Huffman G J, Stocker E F, Bolvin D T, Nelkin E J and Tan J 2023 GPM IMERG final Precipitation L3 1 day 0.1 degree x 0.1 degree V07 *Goddard Earth Sciences Data and Information Services Center (GES DISC)* (https://doi.org/10.5067/GPM/IMERGDF/DAY/07)

Knutti R, Masson D and Gettelman A 2013 Climate model genealogy: generation CMIP5 and how we got there *Geophys. Res. Lett.* **40** 1194–9

Landu K, Leung L R, Hagos S, Vinoj V, Rauscher S A, Ringler T and Taylor M 2014 The dependence of ITCZ structure on model resolution and dynamical core in aquaplanet simulations *J. Clim.* **27** 2375–85

Lang A L, Pegion K and Barnes E A 2020 Introduction to special collection: "bridging weather and climate: subseasonal-to-seasonal (S2S) prediction" *J. Geophys. Res. Atmos.* **125** e2019JD031833

Lang T, Naumann A K, Buehler S A, Stevens B, Schmidt H and Aemisegger F 2023 Sources of uncertainty in mid-tropospheric tropical humidity in global storm-resolving simulations *J. Adv. Model. Earth Syst.* **15** e2022MS003443

Li L, Huang H and Zhu C 2023a Causation of the heavy rainfall in Kyushu in early July 2020: a perspective of the depression that originated over the Tibetan Plateau *Front. Earth Sci.* **11** 1127299

Li P *et al* 2023b Intensification of mesoscale convective systems in the East Asian rainband over the past two decades *Geophys. Res. Lett.* **50** e2023GL103595

Li S, Yang J, Wang X, Zhang R, Gong Z and Feng G 2023c Evaluating and improving the models' prediction skills for the relationship between the summer NWPSH in different months *Geophys. Res. Lett.* **50** e2023GL105485

Li X, Tang Y, Shen Z and Li Y 2023d Spatial variations in seamless predictability of subseasonal precipitation over Asian summer monsoon region in S2S models *J. Geophys. Res. Atmos.* **128** e2023JD038480

Liu B, Yan Y, Zhu C, Ma S and Li J 2020 Record-breaking Meiyu rainfall around the Yangtze river in 2020 regulated by the subseasonal phase transition of the North Atlantic Oscillation *Geophys. Res. Lett.* **47** e2020GL090342

Liu Y, Li W, Zuo J and Hu Z-Z 2014 Simulation and projection of the western pacific subtropical high in CMIP5 models *JMR* **28** 327–40

Nagata R and Mikami T 2017 Changes in the relationship between summer rainfall over Japan and the North Pacific subtropical high, 1901–2000 *Int. J. Climatol.* **37** 3291–6

National Academies of Sciences, Engineering, and Medicine 2016 Next generation Earth system prediction: strategies for subseasonal to seasonal forecasts *National Academies of Sciences* (The National Academies Press) (https://doi.org/10.17226/21873)

Nie J, Fang J and Yang X-Q 2023 The mechanisms of the subseasonal zonal oscillation of the western Pacific subtropical high in 10–25-day period and 25–50-day period *Clim. Dyn.* **60** 3485–502

Pan C, Zhao J, Chen H, Kang Z, Chen S and Jin X 2023 The characteristics of the Yangtze flooding during 1998 and 2020 based on atmospheric water tracing *Geophys. Res. Lett.* **50** e2023GL104195

Ralph F M, Rutz J J, Cordeira J M, Dettinger M, Anderson M, Reynolds D, Schick L J and Smallcomb C 2019 A scale to characterize the strength and impacts of atmospheric rivers *Bull. Am. Meteorol. Soc.* **100** 269–89

Ren H-L *et al* 2023 Seamless prediction in China: a review *Adv. Atmos. Sci.* **40** 1–20

Satoh M, Stevens B, Judt F, Khairoutdinov M, Lin S-J, Putman W M and Düben P 2019 Global cloud-resolving models *Curr. Clim. Change Rep.* **5** 172–84

Schneider T, Teixeira J, Bretherton C S, Brient F, Pressel K G, Schär C and Siebesma A P 2017 Climate goals and computing the future of clouds *Nat. Clim. Change* **7** 3–5

Skamarock W C, Klemp J B, Duda M G, Fowler L D, Park S-H and Ringler T D 2012 A multiscale nonhydrostatic atmospheric model using centroidal voronoi tesselations and C-grid staggering *Mon. Weather Rev.* **140** 3090–105

Song F and Zhou T 2014 Interannual variability of East Asian summer monsoon simulated by CMIP3 and CMIP5 AGCMs: skill dependence on Indian Ocean–western Pacific anticyclone teleconnection *J. Clim.* **27** 1679–97

Stevens B *et al* 2019 DYAMOND: the DYnamics of the atmospheric general circulation modeled on non-hydrostatic domains *Prog. Earth Planet. Sci.* **6** 61

Takaya Y, Ishikawa I, Kobayashi C, Endo H and Ose T 2020 Enhanced Meiyu-Baiu rainfall in early summer 2020: aftermath of the 2019 super IOD event *Geophys. Res. Lett.* **47** e2020GL090671

Tanaka M 1992 Intraseasonal oscillation and the onset and retreat dates of the summer monsoon over east, Southeast Asia and the western Pacific region using GMS high cloud amount data *J. Meteorol. Soc. Japan* II **70** 613–29

Tang S, Luo J-J, He J, Wu J, Zhou Y and Ying W 2021 Toward understanding the extreme floods over Yangtze river valley in June–July 2020: role of tropical Oceans *Adv. Atmos. Sci.* **38** 2023–39

Wang B, Xiang B and Lee J-Y 2013 Subtropical high predictability establishes a promising way for monsoon and tropical storm predictions *Proc. Natl Acad. Sci.* **110** 2718–22

Wang T, Wei K and Ma J 2021 Atmospheric rivers and Mei-yu rainfall in China: a case study of summer 2020 *Adv. Atmos. Sci.* **38** 2137–52

Wang Z, Li M, Zhang S, Small R J, Lu L, Yuan M, Yong J, Lin X and Wu L 2023 The Northern Hemisphere wintertime storm track simulated in the high-resolution Community Earth System Model *J. Adv. Model. Earth Syst.* **15** e2023MS003652

Woolnough S J *et al* 2024 Celebrating 10 years of the subseasonal to seasonal prediction project and looking to the future *Bull. Am. Meteorol. Soc.* **105** E521–E6

Wu J, Li Y, Luo J-J and Jiang X 2021 Assessing the role of air–sea coupling in predicting Madden–Julian oscillation with an atmosphere–ocean coupled model *J. Clim.* **34** 9647–63

Xie P, Joyce R, Wu S, Yoo S H, Yarosh Y, Sun F and Lin R 2019 *NOAA National Centers for Environmental Information* (https://doi.org/10.25921/w9va-q159)

Xu M, Zhao C, Gu J, Feng J, Hagos S, Leung L R, Luo Y, Guo J, Li R and Fu Y 2021 Convection-permitting hindcasting of diurnal variation of Mei-yu rainfall over East China with a global variable-resolution model *J. Geophys. Res. Atmos.* **126** e2021JD034823

Zhou Z-Q, Xie S-P and Zhang R 2021 Historic Yangtze flooding of 2020 tied to extreme Indian Ocean conditions *Proc. Natl Acad. Sci.* **118** e2022255118